

Stellar wind variability in Cygnus X-1 from high-resolution excess variance spectroscopy with Chandra

L. K. Härer^{1,2,*}, M. L. Parker³, I. El Mellah^{4,5}, V. Grinberg⁶, R. Ballhausen^{7,8}, Z. Igo⁹, A. Joyce¹, and J. Wilms¹

¹ Dr. Karl Remeis Sternwarte & Erlangen Centre for Astroparticle Physics, Friedrich-Alexander-Universität Erlangen-Nürnberg, Sternwartstr. 7, 96049 Bamberg, Germany

² Max-Planck-Institut für Kernphysik, Saupfercheckweg 1, 69117 Heidelberg, Germany

³ Institute of Astronomy, Madingley Road, Cambridge, CB3 0HA, UK

⁴ Institut de Planétologie et d'Astrophysique de Grenoble, 414 Rue de la Piscine, 38400 Saint-Martin-d'Hères, France

⁵ Departamento de Física, Universidad de Santiago de Chile, Av. Victor Jara 3659, Santiago, Chile

⁶ European Space Agency (ESA), European Space Research and Technology Centre (ESTEC), Keplerlaan 1, 2201 AZ Noordwijk, The Netherlands

⁷ Department of Astronomy, University of Maryland, College Park, MD 20742

⁸ Center for Research and Exploration in Space Science and Technology, NASA/GSFC, Greenbelt, MD 20771

⁹ Max-Planck-Institut für Extraterrestrische Physik (MPE), Giessenbachstrasse 1, 85748 Garching bei München, Germany

Received 17/04/2023; accepted 19/09/2023

ABSTRACT

Context. Stellar winds of massive stars are known to be driven by line absorption of UV photons, a mechanism which is prone to instabilities, causing the wind to be clumpy. The clumpy structure hampers wind mass-loss estimates, limiting our understanding of massive star evolution. The wind structure also impacts accretion in high-mass X-ray binary (HMXB) systems.

Aims. We analyse the wavelength-dependent variability of X-ray absorption in the wind to study its structure. Such an approach is possible in HMXBs, where the compact object serves as an X-ray backlight. We probe different parts of the wind by analysing data taken at superior and inferior conjunction.

Methods. We apply excess variance spectroscopy to study the wavelength-dependent soft (2–14Å) X-ray variability of the HMXB Cygnus X-1 in the low/hard spectral state. Excess variance spectroscopy quantifies the variability of an object above the statistical noise as a function of wavelength, which allows us to study the variability of individual spectral lines. As one of the first studies, we apply this technique to high-resolution gratings spectra provided by *Chandra*, accounting for various systematic effects. The frequency dependence is investigated by changing the time binning.

Results. The strong orbital phase dependence we observe in the excess variance is consistent with column density variations predicted by a simple model for a clumpy wind. We identify spikes of increased variability with spectral features found by previous spectroscopic analyses of the same data set, most notably from silicon in over-dense clumps in the wind. In the silicon line region, the variability power is redistributed towards lower frequencies, hinting at increased line variability in large clumps. In prospect of the microcalorimetry missions that are scheduled to launch within the next decade, excess variance spectra present a promising approach to constrain the wind structure, especially if accompanied by models that consider changing ionisation.

Key words. accretion, accretion disks – stars: individual: Cygnus X-1 – stars: individual: HDE 226868 – X-rays: binaries – stars: winds, outflows – techniques: spectroscopic

1. Introduction

Accretion onto compact objects is a dynamically complex phenomenon and releases enormous amounts of highly-energetic radiation that strongly impacts the environment of the accretor through feedback processes. The complex dynamics and, in particular, inhomogeneities in the accretion flow often induce variability, which can span many orders of magnitude (e.g., [Os-kinova et al. 2012](#)). Understanding accretion processes on all scales, in galactic and extra-galactic sources, therefore requires precise measurements of both the variability and the environmental characteristics (e.g., densities, ionisations, and element abundances), which calls for a joined spectral and timing analysis.

Excess variance spectroscopy excels at combining spectral and timing information. The excess variance is the variance of

a light curve above the expected statistical noise ([Edelson et al. 2002](#); [Vaughan et al. 2003](#)). If applied to a set of light curves taken in different bands, the spectral distribution of the variability can be studied. Excess variance spectroscopy can reveal the variability behaviour of individual spectral lines, provided sufficient resolution and signal. This presents a clear advantage over other tools, such as colour-colour diagrams ([Nowak et al. 2011](#); [Hirsch et al. 2019](#); [Grinberg et al. 2020](#)). So far, excess variance spectra have mainly been applied to study extra-galactic sources (see, e.g., references in [Parker et al. 2020](#)). In particular, [Parker et al. \(2017a, 2018\)](#) introduced a method to detect ultra-fast outflows of active galactic nuclei (AGN), which are fast wide-angle accretion disk winds. They possess a large amount of mechanical power and therefore influence AGN evolution via feedback processes (e.g., [Tombesi et al. 2010](#)). In recent years, excess variance spectroscopy has proven valuable in detecting ultra-fast outflows and in independently confirming and refin-

* e-mail: lucia.haerer@fau.de

ing known results (Parker et al. 2017a, 2018; Igo et al. 2020; Härer et al. 2021), demonstrating their advantages: excess variance spectra are easy to calculate, provide less biased detections, and show more pronounced features than count spectra. Nevertheless, they have seldom been applied to galactic sources, where high-resolution gratings data present an opportunity to study the wavelength dependence of variability at a resolution above 0.1\AA . We demonstrate the capabilities of excess variance spectroscopy for studying the structure of stellar winds by applying it to *Chandra* observations of the High-Mass X-ray Binary (HMXB) Cygnus X-1 (Cyg X-1).

As binary systems consisting of an O or B star and neutron star or black hole, HMXBs are invaluable laboratories to study accretion, compact objects, and the strong winds of massive stars. Cyg X-1 is one of the most studied HMXBs. As a bright and persistent source, it was discovered in 1964 (Bowyer et al. 1965). The compact object is dynamically constrained to be a black hole (Gies & Bolton 1982) and recently, Miller-Jones et al. (2021) refined the mass estimate to $21.2 \pm 2.2 M_{\odot}$, making Cyg X-1 the most massive known stellar mass black hole in an X-ray binary. The companion star HDE 226868 is an O9.7 Iab supergiant (Walborn 1973) with a mass of $\sim 41 M_{\odot}$ (Miller-Jones et al. 2021). As a blue supergiant star, HDE 226868 has a strong stellar wind with a mass-loss rate of $\sim 10^{-6} M_{\odot} \text{yr}^{-1}$ (Herrero et al. 1995; Gies et al. 2003) and a terminal velocity of $\sim 2100 \text{ km s}^{-1}$ (Herrero et al. 1995). Figure 1 depicts the system and wind geometry of Cyg X-1. The system is seen under an inclination of $27\text{--}28^{\circ}$ (Orosz et al. 2011). Due to the low orbital separation (0.244 AU, Miller-Jones et al. 2021) and short orbital period (5.6 d, Webster & Murdin 1972; Brocksopp et al. 1999; Gies et al. 2003), the donor star is close to filling its Roche lobe, which gives rise to a focused accretion stream along the line connecting the supergiant and the black hole. This geometry was first verified in the optical by Gies & Bolton (1986b,a), with an analysis based on Friend & Castor (1982), and is consistent with X-ray measurements of, e.g., the orbital phase dependence of the column density (see Miškovičová et al. 2016, and references therein).

Winds of massive stars, such as HDE 226868 in Cyg X-1, are driven by resonant line-absorption of stellar UV photons by partly ionised metal ions (Lucy & Solomon 1970; Castor et al. 1975). This physical mechanism is prone to the line-deshadowing instability whose development produces over-dense small scale regions called clumps (Owocki & Rybicki 1984; Owocki et al. 1988; Sundqvist et al. 2018). Most of the wind mass is contained in the clumps, making these winds notoriously inhomogeneous (Hamann et al. 2008; Sundqvist et al. 2012; Puls et al. 2015). Our limited knowledge of wind clumpiness hampers the accuracy of the mass loss rates deduced from all available diagnostics (Fullerton et al. 2006; Sundqvist & Puls 2018). Mass loss, however, plays a key role in the evolution of massive stars, especially in the late stages (Puls et al. 2008). Consequentially, the inaccuracy of mass loss diagnostics limits our understanding of the role radiative, mechanical, and chemical feedback of massive stars plays in many contexts. In HMXBs specifically, the mass loss and the wind structure influence the accretion flow. In’t Zand (2005) first suggested that, in HMXBs, clumpiness could be constrained from the variability of the mass accretion rate onto the compact objects. This claim was challenged by El Mellah et al. (2018) who showed that accreted clumps tend to mix inside the shocked region surrounding the compact object, which smears out the variability induced by stochastic clump capture. Alternatively, the variability of the column density induced by unaccreted wind clumps passing by

the line-of-sight can be used (Oskinova et al. 2012). Motivated by Grinberg et al. (2015), who constrained clump properties in Cyg X-1 with this ansatz, El Mellah et al. (2020), EG20 hereafter, devised a model that connects the statistical properties of the column density variations to the clump size and mass, i.e., the model quantitatively links variability and clump properties.

We apply excess variance spectroscopy to study the stellar wind variability in Cyg X-1. Our aim is both, to test the results obtained previously with an independent approach and to establish excess variance spectroscopy both as an approach for wind studies in HMXBs and as a tool that can be used for high resolution X-ray data, such as obtainable today with the High-Energy Transmission Grating (HETG) on-board *Chandra*, or will become available with the launch of the *XRISM* and *Athena* X-ray missions. We analyse *Chandra*/HETG observations at superior and inferior conjunction of which detailed spectral analysis has been performed in Hanke et al. (2009), Miškovičová et al. (2016), and Hirsch et al. (2019). The existing studies constitute an excellent test case for constraining the stellar wind structure with excess variance spectroscopy and are summarised in Sect. 2. We take advantage of the predictions of column density variability expected in such a system recently introduced by EG20. Section 3 provides more details on the observations, the calculation of the excess variance spectra, the treatment of systematic variability, and the selection of lines we check against. The resulting excess variance spectra and the frequency dependence of the excess variance are shown in Sect. 4. In Sect. 5, we explore the driving mechanism behind the observed variability, model the strong orbital phase dependence based on EG20, and discuss implications for the wind geometry and structure and the role of varying ionisation, before summarising our conclusions in Sect. 6.

2. The clumpy wind in Cyg X-1

Highly variable absorption is observed from Cyg X-1 especially in the low/hard state of the black hole (e.g., Feng & Cui 2002; Ibragimov et al. 2005; Boroson & Vrtilik 2010; Grinberg et al. 2015)¹. In particular, dips in the light curve are observed in soft X-rays preferentially at superior conjunction and interpreted as signatures of the clumps in the wind (see Grinberg et al. 2015, and references therein). At superior conjunction, the line of sight passes closer to the star, potentially sampling a highly structured wind region (see Fig. 1).

A paper series by Hanke et al. (2009), Miškovičová et al. (2016), and Hirsch et al. (2019) used high-resolution *Chandra* spectra to study the wind in the low/hard state in great detail. Hanke et al. (2009) investigated the non-dip spectrum at superior conjunction, identifying absorption lines from several H- and He-like ions and L-shell iron at low velocity shifts. Miškovičová et al. (2016) expanded this study to other orbital phases. They observed P-Cygni line profiles at inferior conjunction, which point to weak absorption and a high projected velocity. As the last paper in the series, Hirsch et al. (2019) investigated the above mentioned absorption dips in the light curve, which are believed to be caused by clumps in the wind. Using time resolved spectra, they studied how absorption from silicon and sulphur ions evolves in the dips, finding that lower ionisation species appear

¹ In the low/hard state, the intrinsic emission from close to the black hole is dominated by a hard, Comptonised component, with comparatively little contribution from the thermal emission of the accretion disk (for a discussion of accretion states in Cyg X-1 see, e.g., Wilms et al. 2006; Grinberg et al. 2013).

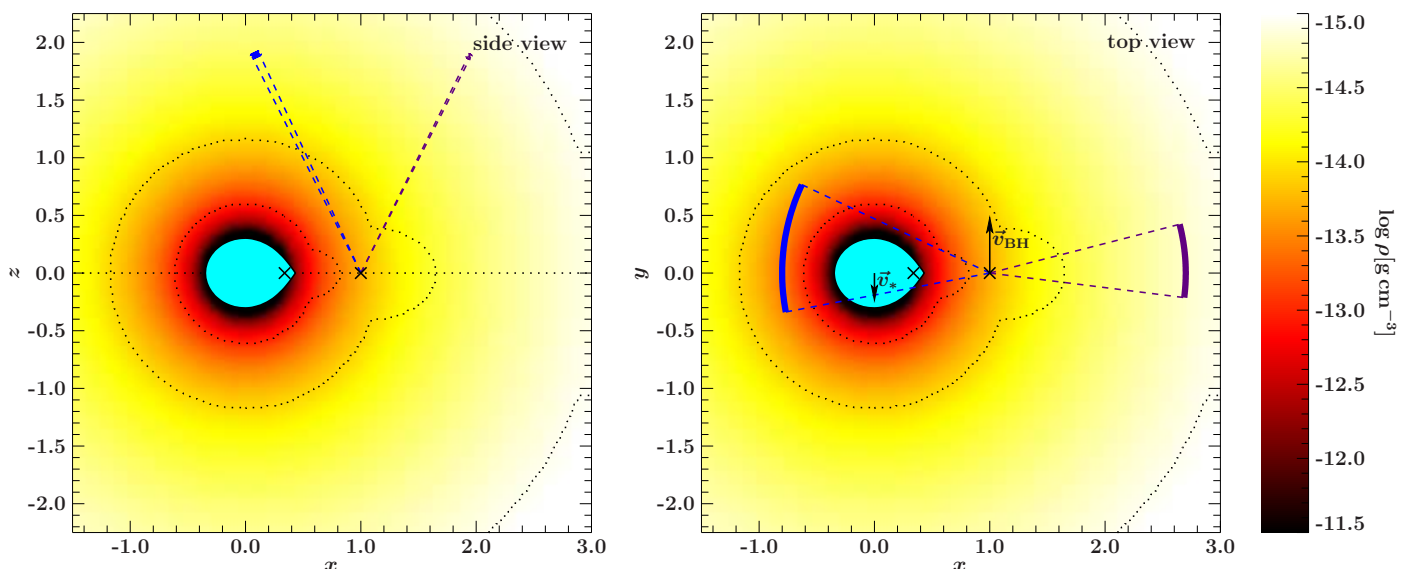


Fig. 1: The density of the stellar wind in Cyg X-1 according to the isotropic clumpy wind model by El Mellah et al. (2020). The average density is shown for clarity, instead of the clumpy wind structure. The dotted contours denote densities of $\log \rho / (\text{g cm}^{-3}) = -13, -14, \text{ and } -15$ in the focused wind model by Gies & Bolton (1986a). The left panel shows a side view (dotted line: orbital plane) and the right a top view (arrows: orbital motion). The line of sight to the black hole and orbital phase covered is highlighted for Obs. 3814 (dashed, blue) and 11044 (dashed, purple). Masses and orbital separation were set according to Miller-Jones et al. (2021).

and increase in relative strength with dip depth. From this result, Hirsch et al. (2019) concluded that material in the clumps has a lower ionisation than its surroundings and that deeper dips correspond to larger clumps. In other words, the clumps have a layered ionisation structure, with large clumps reaching lower ionisations in their centres. An open question that remains from these studies is whether the dips are caused by individual, big clumps passing through the line of sight or by groups of several smaller ones. The geometry (spherical or "pancake"-like) and typical masses also remain to be constrained.

3. Observations and Methods

3.1. Chandra HETG observations of Cyg X-1

We analyse two *Chandra* observations (ObsIDs 3814 and 11044) of Cyg X-1 in the low/hard state taken with the High-Energy Transmission Grating (HETG, Canizares et al. 2005) and the Advanced CCD Imaging Spectrometer (ACIS, Garmire et al. 2003). The observations cover the superior (3814, orbital phase $\varphi = 0.93\text{--}0.03$) and inferior (11044, $\varphi = 0.48\text{--}0.54$) conjunction passages, during which the line of sight probes different parts of the wind (see Fig. 1). At superior conjunction, the line of sight intercepts the wind close to the stellar photosphere and grazes the focused stream. At inferior conjunction, the wind is probed at a greater distance to the companion. Note that the low/hard classification of these observations follows Grinberg et al. (2013) and the orbital phases were assigned according to the ephemeris provided by Gies et al. (2003).

Detailed spectral analysis of both data sets has been performed in the studies mentioned in Sect. 2 (Hanke et al. 2009; Miškovičová et al. 2016; Hirsch et al. 2019). The existing results provide an opportunity to assess the capabilities of our approach against those of conventional analysis techniques. The observations were performed in timed exposure mode (TE), i.e., events are accumulated on the CCDs, transferred in the frame store, and read out. A full read-out cycle of the ACIS-S in TE mode

usually takes 3.2 s, however, in our case the time is halved to 1.7 s, because only 512 of the 1024 available pixel rows were in use. We use the extracted event files provided by Miškovičová et al. (2016), but analyse the entirety of Obs. 3814, including dipping and non-dipping stages. The extractions were created using CIAO version 4.2, consistently with previous work by Miškovičová et al. (2016) and Hirsch et al. (2019) in order to facilitate direct comparison with their spectral results. We include all four first order spectra from the High and Medium Energy Gratings (HEG and MEG, orders ± 1) of the HETG. Refer to Miškovičová et al. (2016) and Hirsch et al. (2019) for further details on the data taking, extraction, and processing.

We perform a spectral and time binning on the extracted events, separately for the four first orders of the HEG and MEG. The spectral binning covers the 2–14 Å band with a 0.05 Å resolution and a 500 s step is used for the time binning. For a closer inspection later on, we increase the spectral resolution threefold and vary the time step in the 50–2000 s range. The excess variance spectrum is then calculated as described in Sect. 3.2. While the spectral resolution and smallest time step are constrained by the signal strength, the maximal time step should be chosen such that the light curve has a sufficient number of bins to obtain an accurate estimate of the variance ($\gtrsim 20$, Vaughan et al. 2003). One sigma uncertainties are given unless otherwise noted.

3.2. Calculating the excess variance spectrum

The excess variance quantifies the variability of an object and is defined as (Edelson et al. 2002; Vaughan et al. 2003):

$$\sigma_{\text{XS}}^2 = S^2 - \overline{\sigma_{\text{err}}^2}, \quad (1)$$

where S^2 is the variance of the light curve and $\overline{\sigma_{\text{err}}^2}$ the arithmetic mean of the squared measurement uncertainty, i.e., the variability introduced by the statistical nature of the measurement process. Subtracting this statistical noise makes the excess variance a quantity which is indicative of only the physical variability of

the source, in other words, if no variability is present, the excess variance is zero. The excess variance depends on source flux, which is avoided by normalising it to the square of the mean number of counts per bin, \bar{x} :

$$F_{\text{var}}^2 = \frac{\sigma_{\text{XS}}^2}{\bar{x}^2}. \quad (2)$$

We write the normalised excess variance in terms of the square of the fractional quantity, F_{var} , also called root mean square (RMS) variability. F_{var} is often used as it is linear in number of counts. However, the squared quantity, F_{var}^2 , is preferable if the variability is low, because F_{var} contains a square root and becomes imaginary if the uncertainty, σ_{err}^2 , is larger than the signal, S^2 . This case is relevant to our analysis because working at gratings resolution makes it necessary to divide the signal over a large number of bins, in comparison to CCD data, to which the excess variance is usually applied.

One advantage of using the excess variance as a measure for variability is the straightforward application to spectral data, i.e., the calculation of an excess variance spectrum. As discussed in the introduction, studying the wavelength dependence of variability can provide unique physical insights that cannot be obtained from static count spectra. To judge the significance of features in the excess variance spectrum, an error estimate is required. We use the expression computed by [Vaughan et al. \(2003\)](#) from a Monte Carlo approach, which accounts for Gaussian and Poissonian measurement uncertainties,

$$\text{err}(F_{\text{var}}^2) = \sqrt{\frac{2\sigma_{\text{err}}^2}{N\bar{x}^2} \left(\frac{\sigma_{\text{err}}^2}{\bar{x}^2} + 2F_{\text{var}}^2 \right)}, \quad (3)$$

where N is the number of photons in the respective bin.

The band pass of frequencies contributing to the excess variance is determined by the time binning of the light curve and the length of the observation. By choosing the time binning, it is therefore possible to probe the frequency dependence of F_{var}^2 and investigate if there is a variability timescale intrinsic to the system. [Hirsch et al. \(2019\)](#) state that the passage of a clump across the line of sight takes 0.5–5 ks, assuming that the observed dips in the spectrum are caused by single clumps and not multiple small clumps. We choose a time step of 500 s for our initial investigation to capture all clump variability in this timescale range. The frequency dependence of the detected features is then investigated in a second step.

3.3. Eliminating systematic variability

As detailed in Sect. 3.1, we analyse *Chandra* HETG data taken with the ACIS-S detector. For a variability study such as that presented in this work, a solid understanding of the timing and read-out properties of the detector and associated systematic effects is vital.

The ACIS-S detector consists of a row of six CCDs, which are read out in sequence. As a consequence, photons arriving simultaneously on different CCDs are registered at slightly different times. This effect becomes relevant if data from multiple gratings or orders, i.e., locations on the detector, are combined. We avoid systematic effects of this kind by calculating F_{var}^2 separately for each grating and order, i , and taking their weighted mean,

$$F_{\text{var}}^2 = \frac{1}{\sum_i \bar{x}_i^2} \sum_i F_{\text{var},i}^2 \cdot \bar{x}_i^2. \quad (4)$$

Weighting by the square of the mean number of counts, \bar{x}_i^2 , gives equal weight to each count, regardless of which grating or order it belongs to. As the errors $\text{err}(F_{\text{var},i}^2)$ are independent, they can be propagated according to

$$\text{err}(F_{\text{var}}^2) = \frac{1}{\sum_i \bar{x}_i^2} \sqrt{\sum_i \bar{x}_i^4 \cdot \text{err}(F_{\text{var},i}^2)^2}. \quad (5)$$

A second systematic effect is the increase in F_{var}^2 due to the photon loss in gaps between CCDs and rows of dead pixels in *Chandra*'s ACIS-S detector. The photon loss is averaged over a range of wavelengths by dithering the telescope pointing², which causes the count rate to vary periodically within dithering range of CCD gaps and dead rows, increasing the variability in this range. In the F_{var}^2 spectrum, this increase manifests itself as spikes at specific wavelengths, which are not per se distinguishable from genuine features. Gap induced F_{var}^2 spikes constitute the largest systematic effect in our analysis, exceeding genuine features up to about an order of magnitude. We detect and filter out affected wavebands separately for each grating and order, before calculating and averaging their $F_{\text{var},i}^2$ as described above. The resulting reductions in sensitivity strongly vary between wavelength bands. For a detailed description, see Appendix A.

While gaps produce spikes at certain wavelength, the discrete nature of the read-out increases the continuum variability for binned spectra. From Monte Carlo simulations detailed in Appendix B, we conclude that the effect on our analysis is negligible but can be significant on timescales approaching the read-out time of the instrument.

3.4. Line selection

We compiled atomic data from various sources to compare to observed features (see Sect. 4). Most of the data was taken from ATOMDB³ and XSTARDB ([Mendoza et al. 2021](#)). The full list of references is shown in Table 1. We only consider transitions from astrophysically abundant elements (e.g., C, N, O, Ne, Mg, Si, S, Fe etc.), which include the ground state. The final selection encompasses 719 lines with energies of 0.1–14.7 keV. For more than one transition at a given wavelength, line identification is based on elemental abundance, oscillator strength, and initial state population. However, fine structure splitting cannot be resolved for most of the lines.

4. Results

4.1. Overview: F_{var}^2 continuum and spike features

Figure 2 shows the F_{var}^2 spectrum for both investigated data sets, Obs. 3814 and 11044, taken during the superior and inferior conjunction passage, respectively, in the 2–14 Å range. A major difference exists between the two: at inferior conjunction, the variability is consistent with zero, while a continuum is present at superior conjunction, which linearly increases with wavelength above ~3 Å. The linear fit shown in Fig. 2 serves to qualitatively characterise this trend and the significance of the superimposed features, the most prominent of which is a spike-like increase in variability just below 7 Å. In contrast, the observation at inferior conjunction shows no clear features.

² <https://cxc.cfa.harvard.edu/proposer/POG/html/ACIS.html> (The *Chandra* Proposer's Observatory Guide, Sect. 6.12)

³ <http://www.atomdb.org>

Table 1: List of spike features in the F_{var}^2 spectrum of Obs. 3814 with a significance $>2\sigma$ and associated lines, which are defined as having a distance of $<0.05\text{\AA}$ to the features. The listed lines are compiled the selection described in Sect. 3.4 and previous analyses of the data: (a) Hanke et al. 2009 and (b) Hirsch et al. 2019. Primary references are numbered and given below.

Spike [\AA]	σ	Ion	Line(s)	Wl. [\AA]	Ref.	Spike [\AA]	σ	Ion	Line(s)	Wl. [\AA]	Ref.
4.37	2.0					9.48	2.1	Fe xxvi	2s \rightarrow 3p	9.536	1
5.30	2.0	S x	L-shell	5.275	5, b	9.50	3.4	Fe xxvi	2p \rightarrow 3d	9.532	1
5.32	2.3							Mg I	K β	9.521	2
6.18	2.5	Si xiv	Ly α	6.182	6, b			Ne x	Ly δ	9.481	4, a
6.65	3.8	Si xiii	i [em.]	6.685	3, b	10.01	2.1	Fe xvii	2s ² 2p ⁶ \rightarrow 2s2p ⁶ 5p	10.102	1
		Si xiii	He α	6.648	3, b			Fe xxv	2s \rightarrow 3p	10.037	1
		Al xii	He β	6.64	a			Na xi	Ly α	10.025	6, a
6.78	2.8	Fe xxiv	2p \rightarrow 7d	6.809	1	10.63	2.2	Fe xix	2p ⁴ \rightarrow 2p ³ 4d	10.664	1
		Fe xxiv	2s \rightarrow 6p	6.787	1			Fe xxiv	2s \rightarrow 3p	10.663	1
		Si xi	L-shell	6.784	5, b			Fe xvii	2p ⁶ \rightarrow 2p ⁵ 6d	10.658	1
		Si I	K β	6.753	2			Ne ix	He ϵ	10.643	8, a
		Fe xxiv	2p \rightarrow 7d	6.751	1			Fe xxiv	2s \rightarrow 3p	10.619	1
		Si xiii	f [em.]	6.740	3, a	11.57	2.8	Na I	K β	11.575	2
		Mg xii	Ly γ	6.738	4			Ne ix	He β	11.546	7, a
6.83	2.3	Si x	L-shell	6.856	5, b			Fe xviii	2p ⁵ \rightarrow 2p ⁴ 4d	11.539	1
6.85	4.5	Fe xxiv	2p \rightarrow 7d	6.809	1			Fe xviii	2p ⁵ \rightarrow 2p ⁴ 4d	11.524	1
		Fe xxiv	2s \rightarrow 6p	6.787	1	12.47	2.1	Fe xx	2p ⁴ \rightarrow 2p ³ 3d	12.475	1
6.90	2.5	Fe xxiv	2p \rightarrow 6s	6.982	1			Fe xxi	2p ² \rightarrow 2p3d	12.445	1
6.92	5.7	Fe xxiv	2p \rightarrow 6d	6.970	1	12.57	2.2	Fe xx	2s ² 2p ³ \rightarrow 2s 2p ³ 3p	12.576	1
6.93	4.4	Si ix	L-shell	6.928	5, b			Fe xxi	2p ³ \rightarrow 2p ² 3d	12.602	1
6.98	2.1	Fe xxiv	2p \rightarrow 6d	7.033	1			Fe xx	2p ⁴ \rightarrow 2p ³ 3d	12.592	1
		Si viii	L-shell	6.996	5, b			Fe xx	2s ² 2p ³ \rightarrow 2s2p ³ 3p	12.570	1
		Fe xxiv	2p \rightarrow 6s	6.982	1			Fe xx	2s ² 2p ³ \rightarrow 2s2p ³ 3p	12.569	1
		Fe xxiv	2p \rightarrow 6d	6.970	1			Fe xx	2s ² 2p ³ \rightarrow 2s2p ³ 3p	12.558	1
8.05	2.2	Fe xxii	2p \rightarrow 5d	8.059	1	12.70	2.3	Fe xxii	2p ² \rightarrow 2p3s	12.710	1
		Na xi	Ly γ	8.021	4, a			Fe xvii	2p ⁶ \rightarrow 2p ⁵ 4s	12.702	1
9.28	2.2	Mg xi	f [em.]	9.314	3, a	12.85	3.2	Fe xx	2p ³ \rightarrow 2p ² 3d	12.867	1
		Ne x	Ly ζ	9.29	a			Fe xx	2p ³ \rightarrow 2p ² 3d	12.809	1
		Ne x	Ly η	9.25	a			Fe xviii	2s ² 2p ⁵ \rightarrow 2s2p ⁵ 3p	12.801	1
		Ne ix	i [em.]	9.23	a						
9.37	3.3	Ne x	Ly ϵ	9.36	a						

References: (1) AtomDB (<http://www.atomdb.org/>), (2) Bearden 1967, (3) Drake 1988, (4) Garcia & Mack 1965, (5) Hell et al. 2016, (6) Johnson & Soff 1985, (7) Liao et al. 2013, (8) Verner et al. 1996. **Notes:** (a) obtain line energies from (1, 8). (5) measure blended line complexes ("L-shell" for short in the table). Lines listed multiple times with different wavelengths differ in the fine structure. Emission lines are marked with [em.]. Iron lines are exclusively from AtomDB.

Figure 3 shows the F_{var}^2 spectrum at superior conjunction for a higher resolution, relative to the linear fit. All data points that lie more than 2σ above a piece-wise running average over 101 bins are highlighted and listed in Tab. 1 with associated transitions. The clear feature seen in Fig. 2 just below 7\AA corresponds to the silicon line region. At the increased resolution, the feature splits into multiple spikes at positions corresponding to those of the lines. A similar group of spikes is seen in the sulphur region, but is less prominent, which is likely due to a reduction in signal caused by gap filtering strongly increasing the uncertainty (see Sect. 3.3 and Appendix A). An alignment of lines and spike features exists outside the silicon and sulphur regions as well: hints of neon (e.g., Ne x Ly δ - η at 9.2 – 9.5\AA), magnesium (e.g., Mg xii Ly γ at 6.74\AA), aluminium (Al xii He β at 6.64\AA), and iron (e.g. at 12.4 – 12.9\AA) features can be seen in Fig. 3. In general, more spikes seem to be present close to known lines than in line-free regions (see black and blue in Fig. 3). However, due to the low signal to noise ratio and strength of the F_{var}^2 features, such detec-

tions are tentative. As previously mentioned, the F_{var}^2 spectrum of Obs. 11044 shows far fewer features. A higher resolution F_{var}^2 spectrum can be found in Fig. C.1 in the appendix.

In Sect. 4.2, we will discuss the silicon and sulphur line regions in Obs. 3814 in more detail, as these contain the most prominent features. Their time dependence will be investigated in Sect. 4.3. As this work is among the first studying F_{var}^2 spectra at gratings resolution (predated only by Mizumoto & Ebisawa 2017, to our knowledge), we aim to assess the prospects of this approach and do not perform a rigorous search and identification of spike features. In addition, a quantitative analysis is challenging, because it requires an accurate description of the continuum.

4.2. Silicon and sulphur line regions at superior conjunction

Figure 4 shows a zoom-in on the silicon and sulphur regions. In addition to the 500 s binning investigated before, a 50 s binning is shown to investigate if there is additional variability at higher

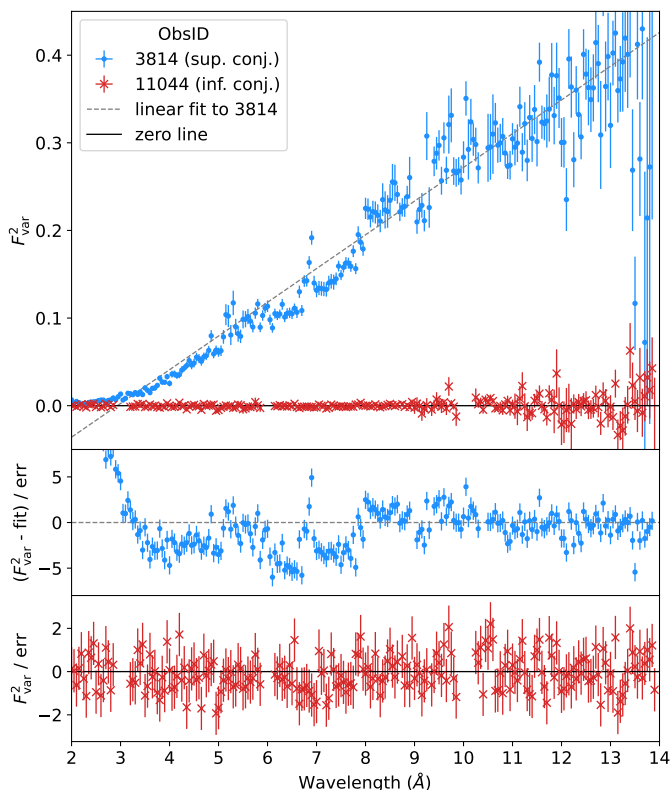


Fig. 2: The F_{var}^2 spectrum of Obs. 3814 (blue) and 11044 (red) during which Cyg X-1 passed through superior and inferior conjunction, respectively. Residuals to a continuum estimate (a linear fit for 3814, the zero-line for 11044) are shown in the bottom panels. The gaps in the F_{var}^2 spectrum of Obs. 11044 around 3Å, 6Å, and 10Å are due to the filtering of systematic variability from CCD gaps in *Chandra*'s HETG detector (see Sect. 3.3 and Appendix A).

frequencies. The bottom panels of Fig. 4 show the count spectra from Hirsch et al. (2019), summed for all dip stages, relative to local powerlaw fits in the given bands, to allow for a direct visual comparison to the F_{var}^2 spectrum.

For silicon, a spike is clearly detected for each corresponding line, except Si xii, which might be because it cancels with the neighbouring He-like Si forbidden emission line. Line emission typically decreases variability, because, when looking at an object, the observer sees the sum of emission from all regions, in which variability in individual regions is averaged out (Parker et al. 2017a). Visually, the spike positions and strengths directly correspond to those of the lines. The asymmetries present in some of the absorption lines in the analyses of the count spectra by Miškovičová et al. (2016) and Hirsch et al. (2019) are also hinted at in the spikes, albeit with greater uncertainties and lower resolution. The heights and widths of the spikes are slightly larger in the 50 s binning, but this increase is not enough to exceed the uncertainty.

The analysis of the sulphur region is complicated by greatly reduced signal, as laid out in Sect. 4.1. Nevertheless, there is a small but visible increase in overall variability. Spike features are resolved and approximately coincide with line positions, with the best agreement for S xi and S xii. S xiii and S xiv cannot be resolved in the F_{var}^2 spectrum, resulting in a joined spike. A spike feature with no corresponding line is present at $\sim 5.33\text{Å}$, but does

not challenge the general conclusion that spike and line positions coincide, due to the large uncertainties and the clear result for silicon. As for silicon, F_{var}^2 slightly increases for the shorter, 50 s time step, but remains within the uncertainty.

4.3. Frequency dependence at superior conjunction

The timescale of the variability can give an insight into its producing mechanism, for example the typical sizes of overdensities in a stellar wind that produces variability by obscuration (e.g., EG20). We investigate this timescale by changing the upper bound of the frequency range F_{var}^2 integrates over, while keeping the lower bound fixed at the length of the observation. In practice, the upper bound is set by the binning time step of the light curves from which F_{var}^2 is calculated (see Sect. 3.2). The result in Fig. 5 therefore effectively shows an integrated frequency spectrum, that is to say, its slope indicates the variability power added to F_{var}^2 at any given frequency.

In the figure, bands containing the bulk of detected silicon (6.6–7.2Å) and sulphur (5–5.35Å) lines are compared to a reference band, spanning the range in between them (5.4–6.6Å), but excluding a region of $\pm 0.05\text{Å}$ around the Si xiv line. The bottom panel shows the ratio of F_{var}^2 in the line regions to the reference band. The F_{var}^2 in each band is rescaled to its value at $t = 500$ s: 0.137 ± 0.001 , 0.105 ± 0.002 , and 0.082 ± 0.004 , for the silicon, sulphur, and the reference band, respectively. Note that these values are not normalised to the linear continuum fit, which means that F_{var}^2 is highest in the silicon region due to the continuum, not the line variability. For the choice of time steps, refer to Sect. 3.1.

Overall, F_{var}^2 declines approximately linearly with binning time step in the logarithmic scaling, which is consistent with an underlying red noise process. The silicon line region shows a flatter trend than the reference band, in other words, the power is distributed more towards lower frequencies in this region. For sulphur, the behaviour is consistent with the continuum, but subject to large uncertainties.

A possible systematic effect is the periodicity of the dither in the telescope pointing. The light grey band in Fig. 5 indicates the range where such an effect would be expected⁴. As no significant increase in F_{var}^2 relative to the overall trend is present in this region, we conclude that the dither periodicity is not an issue in our analysis.

5. Discussion

5.1. Clump driven variability

Variability can be caused by intrinsic changes in flux, originating close to the compact object, or be a result of obscuration by material passing through the line of sight. In the latter case, the variability can be greatly sensitive to the line of sight. We observe that while the continuum variability at superior conjunction increases linearly with wavelength, it is constant and consistent with zero at inferior conjunction. Additionally, while the light curve is constant at inferior conjunction, strong transient dipping events are present at superior conjunction (Miškovičová et al. 2016). It is well established (cf. Sect. 2) that the dipping events are caused by clumps in the stellar wind. During both observations, Cyg X-1 was in the low/hard state at very similar fluxes. Jointly, these results strongly support the conclusion that

⁴ <https://cxc.cfa.harvard.edu/ciao/why/dither.html> (*Chandra* CIAO supplemental information on dither)

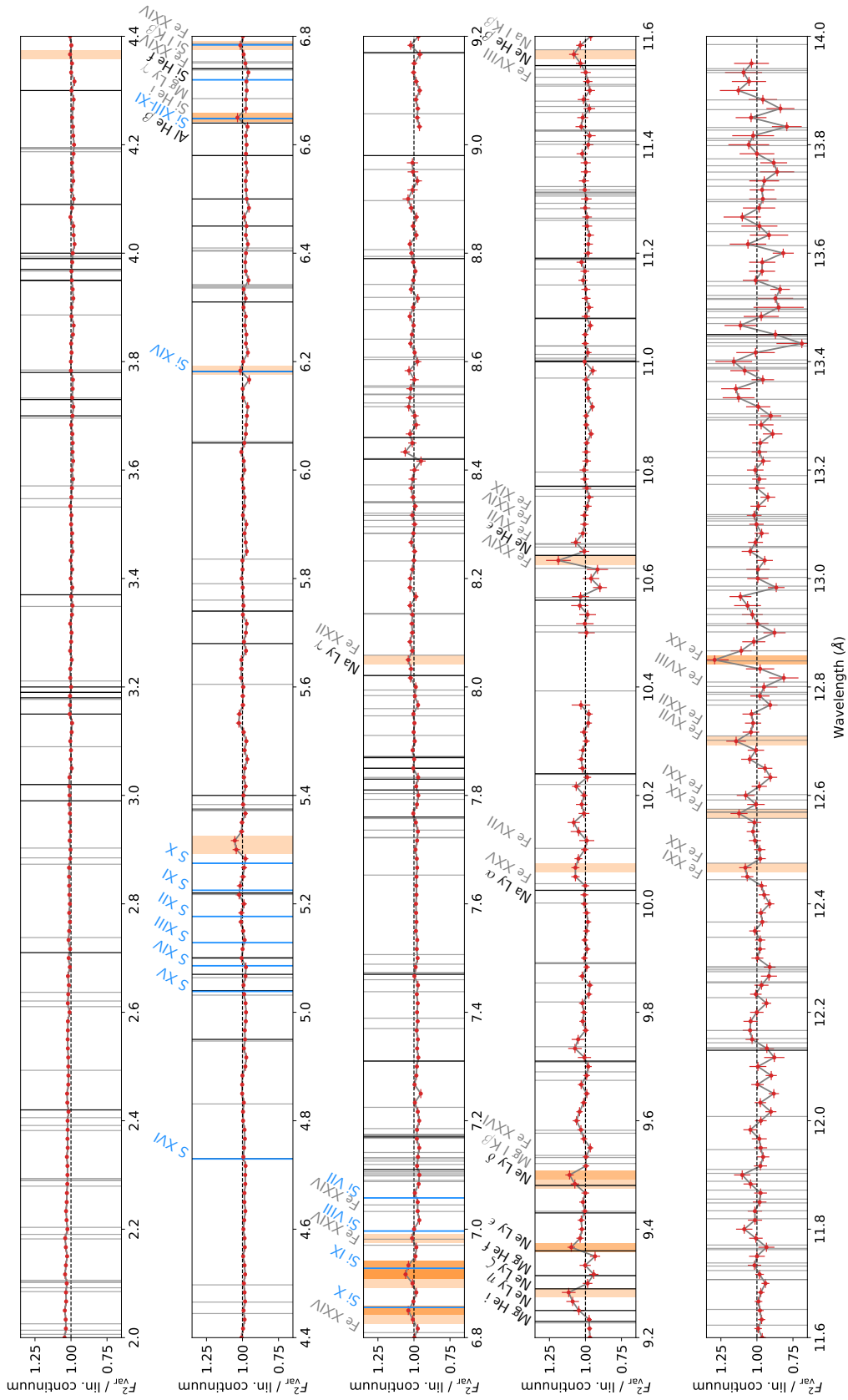


Fig. 3: The F^2_{var} spectrum of Obs. 3814, relative to the continuum fit from Fig. 2. Three sets of lines are shown: H and He-like absorption lines identified by Hanke et al. (2009) (black), S and Si lines from Hirsch et al. (2019) (blue), transitions from the selection described in Sect. 3.4 (grey), which includes iron. Spikes with a significance $\sigma > 2\sigma$ are highlighted in shades of orange according to the value of σ . Lines marked in black and grey are labeled only if they are close ($<0.05\text{Å}$) to a significant spike. For subsequent iron transitions belonging to the same ion the label is shown only once. A list of spikes and associated transitions can be found in Tab. 1.

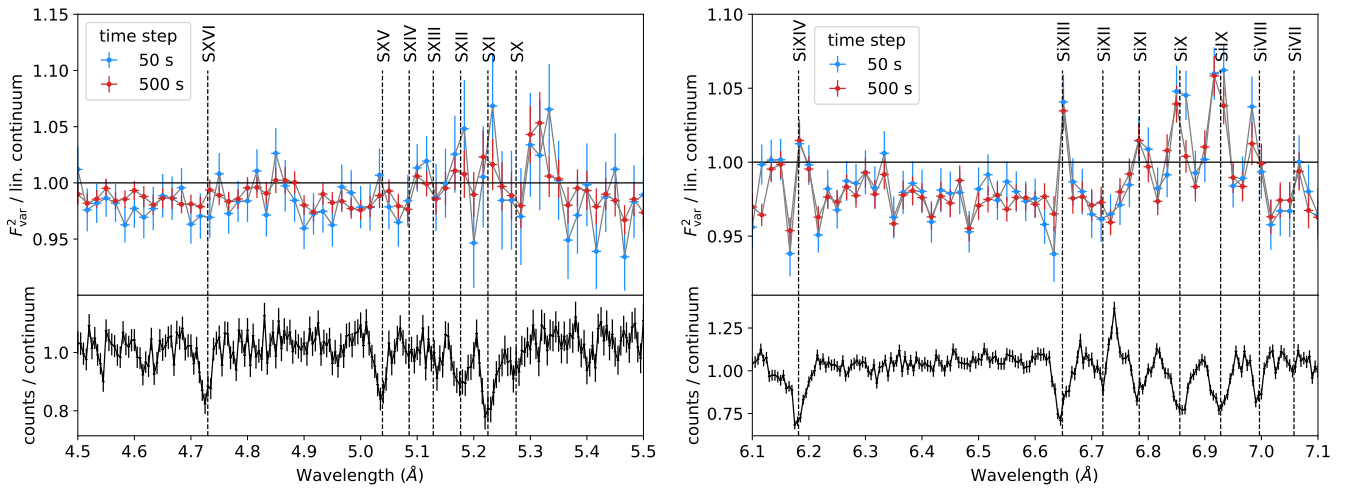


Fig. 4: Sulphur (left) and silicon (right) line regions. The F_{var}^2 spectrum of Obs. 3814 is shown relative to the linear fit from Fig. 2 (black) and compared to the count spectrum (lower panels) from Hirsch et al. (2019) and the rest-wavelength of detected lines. The count spectrum is given relative to a local powerlaw fit, in the wavelength bands indicated in the figure, and is the sum of spectra of all dip stages. Two time binnings are displayed for the F_{var}^2 spectrum, 50 s (blue) and 500 s (red), to investigate the effect of the added higher frequencies. Lines connect the data points for clarity. Overall, there is a good correspondence between F_{var}^2 spike features and known line positions.

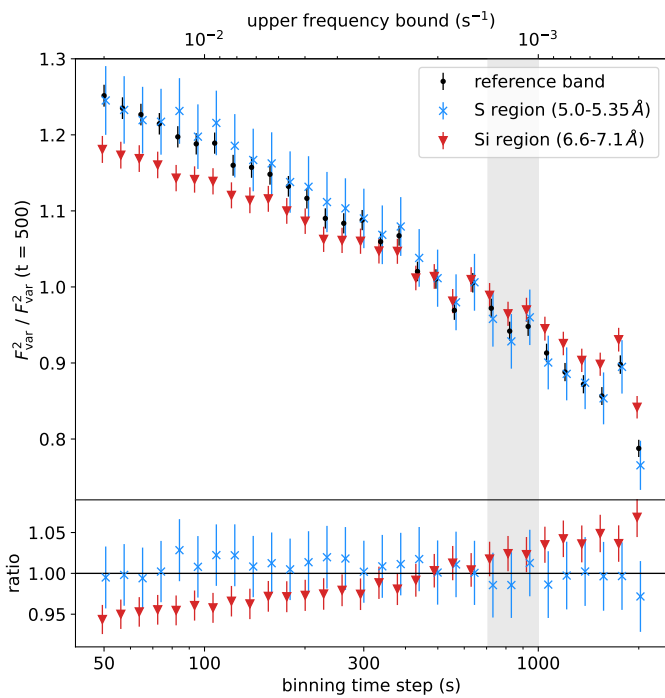


Fig. 5: Total variability in Obs. 3814 in terms of F_{var}^2 as a function of the binning time step, i.e., the figure effectively shows integrated frequency power. The sulphur (blue, 5–5.35 Å) and silicon (red, 6.6–7.2 Å) line regions are compared to a reference band (black, 5.4–6.6 Å, excluding a region of ± 0.05 Å around the Si XIV line), with the ratio shown in the bottom panel. F_{var}^2 is normalised to its value at 500 s in each respective band. The light grey band indicates a range where systematic effects due to the dither of the telescope would arise, if they were present.

the observed variability is driven by clumps crossing the line of sight.

On the continuum, spikes of increased variability are observed, with a clear correspondence between their properties, such as their position and strength, and those of absorption lines in the silicon line region and also, at reduced significance due to lower sensitivity, in the sulphur line region (cf. Sect. 4.2). This result suggests that the spikes are caused by an increased variability inherent to the absorption lines, which is also observed in ultra-fast outflows of AGN (e.g., Parker et al. 2017b, 2018; Igo et al. 2020). A general prevalence of spikes near known lines outside the silicon and sulphur regions further supports this conclusion. Both intrinsic and absorption variability can cause enhanced F_{var}^2 in lines. In ultra-fast outflows, the enhancement is consistent with the ionisation responding to intrinsic luminosity changes (e.g., Pinto et al. 2018; Parker et al. 2020). Considering again that Cyg X-1 has a clumpy wind and that the clumps have a layered ionisation structure (see Sect. 2), it seems plausible that ionisation could also be driving the variability in Cyg X-1. However, in an optically thin medium such as the wind, the line strength can directly respond to a change in the column density, without requiring an associated ionisation change. It is likely that both mechanisms contribute to the observed enhancement of the line variability. The role of ionisation is discussed further in Sect. 5.6.

5.2. Modelling the orbital phase dependent variability of a clumpy stellar wind

In the last section, clumps passing through the line of sight were identified as main driver of the variability. We now compare the results of the F_{var}^2 analysis to a model based on a prescription for a clumpy stellar by EG20. This model does not take into account X-ray photoionisation effects, but instead calculates the total column density of material along the line of sight. We therefore approximate the ionisation effects using an XSTAR (Kallman & Bautista 2001) table model as described below. At the moment, no model exists that simultaneously incorporates both clumping and ionisation.

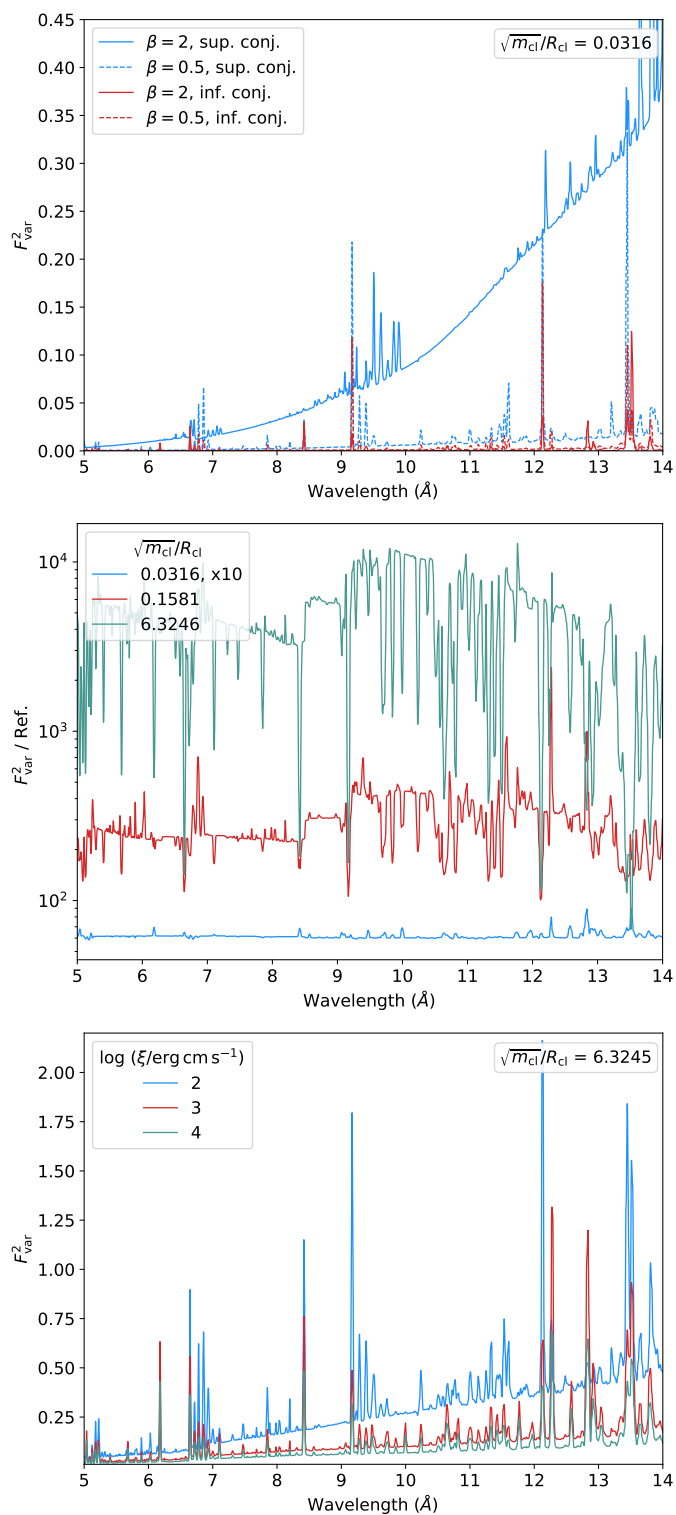


Fig. 6: F_{var}^2 expected for absorption in a clumpy wind following EG20. Details on the model generation can be found in the text. Upper panel: dependence on the line of sight (blue: superior conjunction, red: inferior conjunction) and the β value of the wind velocity law (Eq. 6; solid: $\beta = 2$, dashed: $\beta = 0.5$), highlighting their strong impact on the continuum. Middle panel: ratio to a baseline model with $m_{\text{cl}}^{0.5} R_{\text{cl}}^{-1} = 0.0079$, showing the increase in continuum variability and with $m_{\text{cl}}^{0.5} R_{\text{cl}}^{-1}$ and the reduced increase of the line variability (dips in the ratio). The lowest-ratio model (blue) has been multiplied by a factor of 10 for better visibility. Bottom panel: ionisation dependence. A high $m_{\text{cl}}^{0.5} R_{\text{cl}}^{-1} = 6.3245$ is shown to highlight the continuum changes. The increase in F_{var}^2 with ionisation is weaker for higher ionisations. For clarity, the model is only shown above 5\AA .

EG20 model the X-ray absorption by a clumpy wind in a binary system consisting of a massive star and a compact object, described as an X-ray point source. The mass is assumed to be contained in spherical clumps, with a radius R_{cl} at two stellar radii, $2R_{\star}$, from the stellar centre, growing in size and accelerating as they move outwards according to the canonical velocity law for stellar winds,

$$v(r) = v_{\infty}(1 - R_{\star}/r)^{\beta}, \quad (6)$$

where β is a factor determining how quickly the terminal wind velocity, v_{∞} , is reached. We employ the smooth expansion law for the clump size (Eq. 4 in EG20) but note that the impact of the clump expansion law on the variability is expected to be small (see EG20). The wind is assumed to be spherically symmetric and fast enough to be unaffected by the gravity of the compact object, which is a valid assumption for Cyg X-1 for two reasons: the terminal wind speed (2100 km s^{-1}) is high compared to the orbital speed (500 km s^{-1}) and more importantly, the bulk of material intercepting the line of sight is above the orbital plane.

The model calculates the total equivalent hydrogen column density, N_{H} , resulting from the clumpy wind for a given line of sight parameterised by the inclination, i , and orbital phase, φ , without taking into account possible ionisation effects. We adopt the parameters that EG20 give for Cyg X-1: $i = 27.1^{\circ}$, mass outflow rate, $\dot{M} = 3 \cdot 10^{-6} M_{\odot} \text{ yr}^{-1}$, $v_{\infty} = 2100 \text{ km s}^{-1}$, and orbital separation, $a = 2.5 R_{\star}$. Orbital phases of ± 0.1 around superior and inferior conjunction are covered, with a resolution of 20000 points, resulting in a time step of ~ 5 s. For further details on the model and its application to Cyg X-1 see EG20.

The N_{H} light curve obtained from the clumpy wind model is then used to create absorbed model spectra, from which F_{var}^2 can be calculated. We do this by faking an absorbed powerlaw for each value in the N_{H} light curve with the `isis` command `fakeit`. The powerlaw index and normalisation were fixed to the values obtained by Hanke et al. (2009) for the *Chandra* and *RXTE* joined continuum of Obs. 3814 ($\Gamma = 1.60$, $\text{norm} = 1.33$, see Tab. 2 in the reference). For the absorption, we use a custom `xstar` table model, following the approach detailed in Hirsch et al. (2019). The model is based on a calculation of the ionisation balance in a spherical gas cloud irradiated from the centre. The SED describing the source of incident continuum at the centre of the cloud includes a `nthcomp` continuum model, combined with lamp-post model relativistic reflection (`relxillpcp`) and a small contribution from a non-relativistic reflection (`xillvercp`). The model reflects the idea that the primary X-ray radiation of the BH is already reprocessed by reflection of the accretion disk before interacting with the stellar wind of the donor. For this study, we chose $\Gamma = 1.67$, $kT_e = 400 \text{ keV}$, and inclination of $36^{\circ 5}$ for both reflection components. The height of the primary component in the `relxillpcp` component is $6.1 r_g$ and the spin of the BH is 0.998. The ionization parameters $\log \xi$ are 3.1 and 0, for `relxillpcp` and `xillvercp`, respectively, and the reflection fractions are 0.27 and -1^6 . The reflection parameters represent a reasonable assumption for the conditions in Cyg X-1 in the typical hard state. The results of

⁵ A misalignment of the inner disk inclination to the inclination of the system has been inferred for Cyg X-1 in several studies when not using high density reflection models (Tomsick et al. 2014; Parker et al. 2015; Walton et al. 2016; Tomsick et al. 2018) and is also supported by polarimetry measurements (Krawczynski et al. 2022). The value we employ here corresponds to the measurements of inner disk inclination in the hard state in Tomsick et al. (2018).

⁶ See <http://www.sternwarte.uni-erlangen.de/~dauser/research/relxill/> for the definition of the parameters.

our qualitative discussion, which is concerned with the overall effects of ionisation, are not sensitive to slight changes in the conditions.

The F_{var}^2 spectra resulting from this approach are shown in Fig. 6. We investigate the dependence on β , the line of sight, the ionisation parameter of the xstar model⁷, ξ , and the ratio $m_{\text{cl}}^{0.5}R_{\text{cl}}^{-1}$, where m_{cl} and R_{cl} are given as multiples of $m_0 = 1.1 \cdot 10^{18}$ g and $R_{\star} = 17 R_{\odot}$ ⁸. The clump mass, m_{cl} , takes values of 0.4 and 10 and R_{cl} ranges over 0.005–0.08. This range overlaps with the result of Feng & Cui (2002) ($R_{\text{cl}} = 0.01$ –0.6), who obtained clump sizes by analysing the duration of the dips in the light curve. The choice of the combined parameter $m_{\text{cl}}^{0.5}R_{\text{cl}}^{-1}$ is motivated by EG20, who found that it is proportional to the spread of the column density, δN_{H} . If variability is caused by N_{H} changes, as our model assumes, then δN_{H} directly translates in F_{var}^2 variability. We consider two values for β , 0.5 and 2. The former is widely used in the literature and believed to be representative of winds of early O supergiants (Sundqvist et al. 2019), while the latter corresponds to the velocity profiles computed by Sander et al. (2018), showing a more gradual acceleration. Unless otherwise indicated, the ionisation is fixed at $\log \xi = 3$, $\beta = 0.5$, and variability at inferior conjunction is shown. The ionisation, ξ , is always given in units of erg cm s^{-1} .

5.3. Line of sight dependence of the variability continuum

The employed model is able to qualitatively reproduce the data, by predicting an approximately linear continuum and spikes of increased F_{var}^2 (Fig. 6, upper panel). The model also shows a strong line of sight effect, with higher variability at superior conjunction. The effect is especially strong for the higher β value, $\beta = 2$, and is a direct consequence of how δN_{H} depends on the orbital phase. The clumps probed at superior conjunction are smaller, because the line of sight runs closer by the star than at inferior conjunction and the clumps expand as they move outwards. As $\delta N_{\text{H}} \propto m_{\text{cl}}^{0.5}R_{\text{cl}}^{-1}$, the variability is higher at superior conjunction if the clump mass is fixed. A high β increases this effect, because the slower acceleration requires a higher density if $\dot{M} = \text{const.}$ and therefore more clumps. The variability increases with wavelength, because lower energy photons are more sensitive to changes in absorption.

For $\beta = 2$ and $m_{\text{cl}}^{0.5}R_{\text{cl}}^{-1} = 0.0316$, the model predicts $F_{\text{var}}^2 \sim 0.37$ at 14\AA at superior conjunction and an inferior conjunction continuum that is consistent with zero within the measurement accuracy. These values agree very well with the measurement (Fig. 2). However, the slope of the superior conjunction continuum is too steep, which causes F_{var}^2 to be underestimated below 14\AA . Larger $m_{\text{cl}}^{0.5}R_{\text{cl}}^{-1}$ reduce this discrepancy, but require a non-zero inferior conjunction continuum.

The fact that the model is able to reproduce the qualitative behaviour of the data consistently at both conjunctions shows that varying absorption in an ionised clumpy wind is a viable explanation for the observed variability. Discrepancies, such as mentioned above, are expected given that the model is in an early state and we thus discuss two noteworthy model caveats and their effect on the variability continuum and line of sight dependence. First is the spherical wind assumption, which disregards the focused stream between star and black hole, whose higher density

could lead to an increase in variability at superior conjunction. At inferior conjunction, the line of sight passes through the bow shock trailing the black hole, which could disrupt the wind structure and smooth out the absorption variability. A similar effect is expected from interaction with the jet, through which the wind inevitably passes before crossing the inferior conjunction line of sight. Perucho & Bosch-Ramon (2012) showed that wind structures are usually destroyed in interactions with a jet. Second is the use of the canonical velocity law (Eq. 6), especially considering that the wind is ionised by the X-ray emission from the black hole, resulting in a change in the populations of the driving lines. The X-ray luminosity in Cyg X-1 ($L_{\text{x}} \gtrsim 10^{37}$ erg s⁻¹, Miškovičová et al. 2016; Hirsch et al. 2019) is in a regime where it could significantly inhibit the wind acceleration (Krtićka et al. 2018), although the net effect of X-ray photoionising feedback is still uncertain (see Sander et al. 2018, for the insightful example of Vela X-1, another HMXB). The inhibiting effect would be largest towards the black hole where the X-ray irradiation is strongest. It could therefore increase F_{var}^2 at superior conjunction, as a slower wind must have a higher density if \dot{M} is fixed. Even without an ionising source, Sander et al. (2017) predict a slower onset of the acceleration, from a model that calculates a self-consistent hydrodynamic stratification of the wind.

5.4. Suppressed line variability at inferior conjunction

The line variability predicted by the model is of a similar strength at superior and inferior conjunction (Fig. 6, upper panel), yet the observations show line variability only at superior conjunction. This discrepancy is due to the wind moving and becomes apparent from the discussion of the count spectra in Miškovičová et al. (2016). While the superior conjunction spectrum shows absorption, mainly P-Cygni profiles are observed at inferior conjunction. Miškovičová et al. (2016) ascribe this difference to the fact that the absorption at inferior conjunction is highly blue-shifted, because of the line of sight projection of the wind velocity, separating it from the ubiquitous emission component. Emission lines are suggested to reduce F_{var}^2 instead of increasing it (Parker et al. 2017b). It is likely that the variability of the absorption and emission components cancels out, given that the absorption component is weak at inferior conjunction and that our resolution is lower than that of the count spectra. In addition, narrow spikes appear smaller at lower resolution, because of the averaging effect. The resolution effect also applies at superior conjunction, and plausibly explains why the reported variability is slightly lower than in the model (compare the F_{var}^2 spikes in Fig. 2 and Fig. 6, upper panel).

5.5. Clump mass and radius

The middle panel of Fig. 6 shows the behaviour of our model with $m_{\text{cl}}^{0.5}R_{\text{cl}}^{-1}$, by taking a low value as a baseline (0.0079; big, light clumps: $m_{\text{cl}} = 0.4 m_0$, $R_{\text{cl}} = 0.08 R_{\star}$) and showing the ratio of models with higher values to it. As mentioned in Sect. 5.2, $m_{\text{cl}}^{0.5}R_{\text{cl}}^{-1}$ is proportional to δN_{H} and therefore also to F_{var} . For the investigated ratios, the variability spans several orders of magnitude, making $m_{\text{cl}}^{0.5}R_{\text{cl}}^{-1}$ an influential parameter. For low ratios, the increase in the lines is stronger than in the continuum (light blue curve), but as higher ratios are approached, the increase is reduced (dips in the red and green curves). This relative reduction in line variability is an averaging effect. As $m_{\text{cl}}^{0.5}R_{\text{cl}}^{-1} \propto \delta N_{\text{H}}$, the absorption varies over a larger range for higher values of the ratio. Less absorbed spectra are brighter and therefore have a

⁷ As defined by Tarter et al. (1969): $\xi = L_{\text{x}}\rho^{-1}r^{-2}$.

⁸ Note that we adopt the stellar radius given in EG20 here, instead of the updated value of $R_{\star} = 22.3 R_{\odot}$ (Miller-Jones et al. 2021). The results are unaffected by this slight inconsistency, because R_{\star} only functions as a scaling factor for the $m_{\text{cl}}^{0.5}R_{\text{cl}}^{-1}$ ratio.

higher weight in the average that is contained in the definition of F_{var}^2 (see Eq. 1 and 2). They also show weaker lines, because the line strength responds to the absorbing column. As a consequence, the line variability relative to the continuum is weaker for higher δN_{H} , resulting in the dips in the model ratio. In addition to this effect, the continuum variability gets more linear, as seen by comparing the upper to the bottom panel in Fig. 6, where a high $m_{\text{cl}}^{0.5} R_{\text{cl}}^{-1}$ ratio was chosen.

An independent approach to obtain information on R_{cl} is measuring the timescale of the variability, as small structures cross the line of sight more quickly than large ones, causing the timescale to depend on R_{cl} . Our analysis of the time binning dependence in Sect. 4.3 revealed that the distribution of variability power is shifted towards lower frequencies in the silicon line region compared to the continuum. Such a result is explained by the response of the line region to the column density changes driving the variability: the line depths vary across a wider range in bigger clumps, which enhances their variability and therefore flattens the frequency trend. This mechanism is likely complemented by the layered ionisation structure of the clumps. Bigger clumps allow for a lower ionisation in their centre (see Sect. 2), which also increases the range across which line depths vary. In addition, the larger ionisation range gives rise to more lines. This interpretation is in line with our conclusion from Sect. 5.1 that column density changes might drive ionisation variability. As a general conclusion, timescale measurements can independently reveal m_{cl} and R_{cl} , if $m_{\text{cl}}^{0.5} R_{\text{cl}}^{-1}$ can be constrained. In principle, the clump size can also be obtained from the duration of dips in the light curve, as demonstrated, in Feng & Cui (2002) and Ness et al. (2012). In case of Cyg X-1, the necessity to account for the orbital speed, the progressive acceleration of the wind, and projection effects complicates this approach (see discussion in EG20).

5.6. Ionisation

The bottom panel of Fig. 6 shows F_{var}^2 model spectra for $\log \xi = 2-4$ (the $m_{\text{cl}}^{0.5} R_{\text{cl}}^{-1}$ ratio was chosen to be high in this plot to explicitly show the continuum changes.). Ionisation acts mainly as a scaling factor for both the continuum and line variability. The effect is stronger at lower ionisations.

We therefore do not expect the choice of $\log \xi = 3$ to impact the conclusions we reached so far. To illustrate the effect of ξ on spectral features in more detail, we show Fe ion abundances from an xSTAR photoionisation model in Fig. 7. The lower x-axis shows the maximum value of ξ reached in the absorber. The corresponding minimum distance of the absorber from the X-ray source (upper x-axis) is obtained by inverting the definition of ξ (Tarter et al. 1969),

$$d = \sqrt{\frac{L_{\text{X}}}{\xi \rho}}, \quad (7)$$

where $L_{\text{X}} = 10^{37} \text{ erg s}^{-1}$ for Cyg X-1 and ρ is taken from the clumpy wind model by EG20 evaluated at superior conjunction (adopting $\beta = 2$ and a mean molecular weight of $\mu = 1 \text{ u}$). Miškovičová et al. (2016) estimate the distance between absorber and black hole to be $d \lesssim 0.25 a$, which gives $\log \xi \gtrsim 1.8$. This lower limit does not constrain the ion abundances well (see Fig. 7) and a conclusion on which lines dominate the spectrum is difficult to draw without better constraints on the absorber position. Considering that the absorber likely has a significant extent, is clumpy and that the ion abundances strongly depend on ξ (see Fig. 7), it is expected to have a complex ionisation structure.

Despite the discussed limitations, fixing the ionisation to a single value has proven to be a successful first step, considering the good qualitative agreement of data and model. However, this simple approach inevitably results in an incomplete picture, because varying ionisation is known to contribute to the variability (see Sect. 5.1) and even the clumps themselves have a layered ionisation structure. Examples for the behaviour that might arise from this structure were given in Sect. 5.1 and 5.5.

In the general case, the response of variability to changes in ξ is non-trivial: for example, variability in absorption lines is not necessarily enhanced. The decisive question is how it correlates with the continuum variability. If line strength decreases with increasing flux, the total flux change is higher in the line than in the continuum, causing F_{var}^2 to spike. In the contrary case, the change in the line counteracts that in the continuum, resulting in an F_{var}^2 dip. For ionisation-driven variability, both cases are possible, even within the same observation because a change in ionisation shifts the ion balance, which means that abundances rise for some ions while they decrease for others. Only in specific regimes can the situation be simpler: for example, in an almost fully ionised environment, the responses of the lines to ionisation changes are more uniform. This special case is thought to apply to ultra-fast outflows of AGN and result in the observed anticorrelation between line strength and flux (Parker et al. 2017b, 2018; Igo et al. 2020). In Cyg X-1, the situation is likely to be complex, because of the wide range of ionisations. Adding to that, lines can show different responses in different regions in the source from which we observe the sum, as we argued in Sect. 5.4 for P-Cygni profiles. As a result of this complex behaviour, a comprehensive model will require radiative transfer modelling, which is outside the scope of this work.

6. Summary and Outlook

We presented an analysis of high resolution excess variance spectra of Cyg X-1 calculated from *Chandra*/HETG observations during the low/hard state at superior and inferior conjunction (ObsID 3814 and 11044, respectively), which enabled us to discuss the impact of the accretion geometry and wind structure on the excess variance. We match features in the excess variance to their counterparts in the count spectra comparing to previous spectral analysis by Hanke et al. (2009), Miškovičová et al. (2016), and Hirsch et al. (2019) and to a selection of significant iron lines in the 2–14 Å range. To complement the data analysis, we modelled excess variance spectra from X-ray absorption in a clumpy stellar wind based on EG20 and an xSTAR table model to incorporate ionisation effects.

We have demonstrated that we can deal with systematic variability introduced by the use of *Chandra* gratings data, by accounting for photon loss in CCD gaps, differences in the effective areas of the gratings arms, the discreteness of the CCD read-out cycle, and the telescope dither. The fact that the inferior conjunction variability is consistent with zero and shows no features rules out the existence of further systematic effects that would increase the variability at a measurable level, highlighting the reliability of our results.

Overall, this work demonstrates that excess variance can be used to study winds of HMXBs, providing an independent new approach to previous high resolution spectral studies. Our main conclusions are:

1. The excess variance is strongly dependent on the orbital phase with a linearly increasing continuum and spike fea-

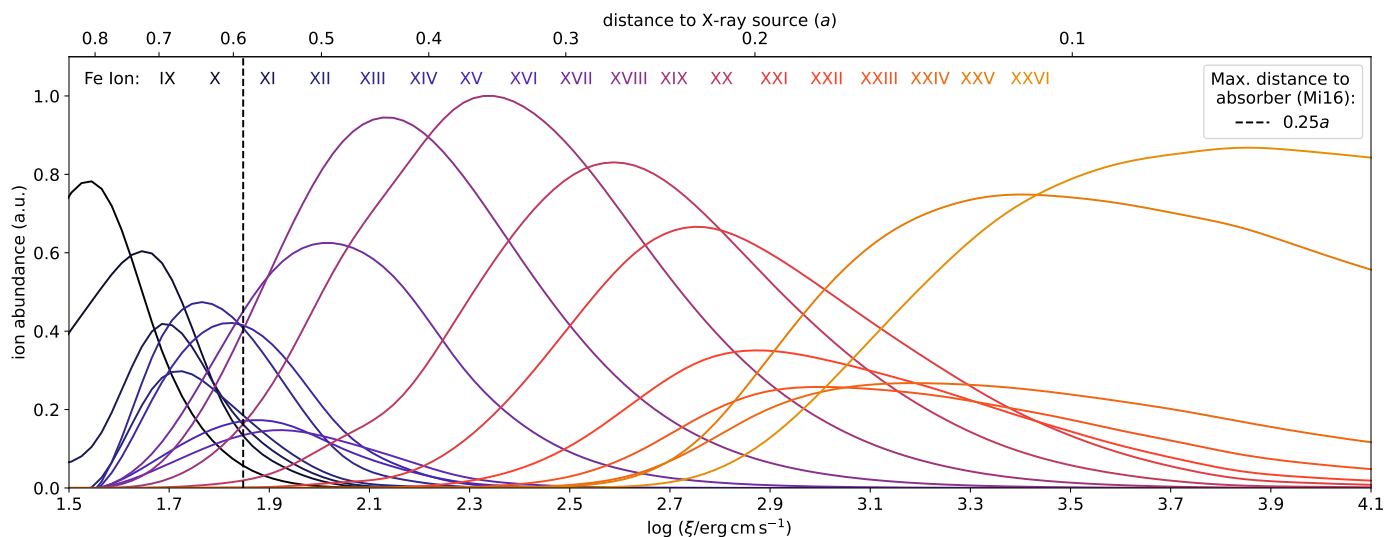


Fig. 7: Relative abundances of iron K to M-shell ions as a function of the ionisation parameter, ξ (lower x-axis) or, equivalently, the distance absorber–X-ray source, d (upper x-axis). The dashed line marks the maximum value of d according to Miškovičová et al. (2016), given in terms of the semi-major axis of the binary system, $a = 2.35 R_\star$ (Miller-Jones et al. 2021). For details, see Sect. 5.6.

tures at superior conjunction and the inferior conjunction spectrum consistent with zero.

2. Modelling shows that the variability is consistent with changes in column density caused by clumps crossing the line of sight. The orbital phase dependence is slightly under-predicted and a slowly accelerating wind is required. We suggest that the jet or the bow shock of the black hole in the focused wind disrupts the wind structure, suppressing inferior conjunction variability, and name effects that might increase superior conjunction variability.
3. Variability in absorption lines is enhanced at superior conjunction, with this effect being especially clear in the silicon and sulphur line regions. We suggest that no significant variability spikes are seen at inferior conjunction, because the projected wind velocity is higher, causing the count spectrum to be dominated by P-Cygni profiles, whose absorption and emission components cancel out in variability.
4. The variability power in the silicon region is redistributed towards lower frequencies, compared to the nearby continuum. We argue that the line variability might be increased in big clumps, which have higher column densities and reach lower ionisations in their centres.

We have discussed that the impact of ionisation is highly non-trivial, calling for radiative transfer simulations. In future work, we aim to generate an F_{var}^2 table model for clumpy stellar winds including improvements such as this one. Such a model will allow us to constrain the clump mass-size ratio, $m^{0.5} R_{\text{cl}}^{-1}$, which constitutes a direct approach to quantify the wind structure, when combined with an F_{var}^2 timescale analysis, the feasibility of which we have demonstrated.

This outlook highlights that excess variance spectra are a versatile tool, first and foremost, because they manage to combine spectral and timing information, making it easy to handle and model. In addition, excess variance features tend to be more pronounced than those in count spectra (compare the height of the silicon F_{var}^2 spike to the continuum in Fig. 2), which is in line with previous results laid out in Sect. 1. This emphasizes the importance of establishing this analysis method for the future missions. The results presented here also present a sneak peak

at the detail with which extra-galactic sources will be able to be studied with microcalorimetry. The major challenge, and the reason why few studies have applied excess variance spectroscopy to data of high spectral resolution, is the amount of signal required to perform simultaneous energy and time binning. Within the next decades, microcalorimetry instruments such as *XRISM* (Tashiro et al. 2018) and *Athena* (Nandra et al. 2013) will become available that solve this issue for a range of sources. The technical difficulties we faced in this work come almost exclusively from the use of gratings and will naturally disappear when switching to microcalorimetry.

Acknowledgements. LH was supported by the European Space Agency (ESA) trainee programme. IEM has received funding from the European Research Council (ERC) under the European Union’s Horizon 2020 research and innovation programme (SPAWN ERC, grant agreement No 863412). RB acknowledges support by NASA under award number 80GSFC21M0002.

References

- Bearden, J. A. 1967, *Reviews of Modern Physics*, 39, 78
- Boroson, B. & Vrtilek, S. D. 2010, *ApJ*, 710, 197
- Bowyer, S., Byram, E. T., Chubb, T. A., & Friedman, H. 1965, *Annales d’Astrophysique*, 28, 791
- Brocksopp, C., Fender, R. P., Larionov, V., et al. 1999, *MNRAS*, 309, 1063
- Canizares, C. R., Davis, J. E., Dwey, D., et al. 2005, *PASP*, 117, 1144
- Castor, J. I., Abbott, D. C., & Klein, R. I. 1975, *ApJ*, 195, 157
- Drake, G. W. 1988, *Canadian Journal of Physics*, 66, 586
- Edelson, R., Turner, T. J., Pounds, K., et al. 2002, *ApJ*, 568, 610
- El Mellah, I., Grinberg, V., Sundqvist, J. O., Driessen, F. A., & Leutenegger, M. A. 2020, *A&A*, 643, A9
- El Mellah, I., Sundqvist, J. O., & Keppens, R. 2018, *MNRAS*, 475, 3240
- Feng, Y. X. & Cui, W. 2002, *ApJ*, 564, 953
- Friend, D. B. & Castor, J. I. 1982, *ApJ*, 261, 293
- Fullerton, A. W., Massa, D. L., & Prinja, R. K. 2006, *ApJ*, 637, 1025
- Garcia, J. D. & Mack, J. E. 1965, *Journal of the Optical Society of America* (1917–1983), 55, 654
- Garmire, G. P., Bautz, M. W., Ford, P. G., Nousek, J. A., & Ricker, George R., J. 2003, in *Society of Photo-Optical Instrumentation Engineers (SPIE) Conference Series*, Vol. 4851, X-Ray and Gamma-Ray Telescopes and Instruments for Astronomy., ed. J. E. Truemper & H. D. Tananbaum, 28–44
- Gies, D. R. & Bolton, C. T. 1982, *ApJ*, 260, 240
- Gies, D. R. & Bolton, C. T. 1986a, *ApJ*, 304, 389
- Gies, D. R. & Bolton, C. T. 1986b, *ApJ*, 304, 371
- Gies, D. R., Bolton, C. T., Thomson, J. R., et al. 2003, *ApJ*, 583, 424

- Grinberg, V., Hell, N., Pottschmidt, K., et al. 2013, *A&A*, 554, A88
- Grinberg, V., Leutenegger, M. A., Hell, N., et al. 2015, *A&A*, 576, A117
- Grinberg, V., Nowak, M. A., & Hell, N. 2020, *A&A*, 643, A109
- Hamann, W.-R., Feldmeier, A., & Oskinova, L. M. 2008, in *Clumping in Hot-Star Winds*
- Hanke, M., Wilms, J., Nowak, M. A., et al. 2009, *ApJ*, 690, 330
- Härer, L., Parker, M. L., Joyce, A., et al. 2021, *MNRAS*, 500, 4506
- Hell, N., Brown, G. V., Wilms, J., et al. 2016, *ApJ*, 830, 26
- Herrero, A., Kudritzki, R. P., Gabler, R., Vilchez, J. M., & Gabler, A. 1995, *A&A*, 297, 556
- Hirsch, M., Hell, N., Grinberg, V., et al. 2019, *A&A*, 626, A64
- Ibragimov, A., Poutanen, J., Gilfanov, M., Zdziarski, A. A., & Shrader, C. R. 2005, *MNRAS*, 362, 1435
- Igo, Z., Parker, M. L., Matzeu, G. A., et al. 2020, *MNRAS*, 493, 1088
- in't Zand, J. J. M. 2005, *A&A*, 441, L1
- Johnson, W. R. & Soff, G. 1985, *Atomic Data and Nuclear Data Tables*, 33, 405
- Kallman, T. & Bautista, M. 2001, *ApJS*, 133, 221
- Krawczynski, H., Muleri, F., Dovčiak, M., et al. 2022, *Science*, 378, 650
- Krtička, J., Kubát, J., & Krtičková, I. 2018, *A&A*, 620, A150
- Liao, J.-Y., Zhang, S.-N., & Yao, Y. 2013, *ApJ*, 774, 116
- Lucy, L. B. & Solomon, P. M. 1970, *ApJ*, 159, 879
- Mendoza, C., Bautista, M. A., Deprince, J., et al. 2021, *Atoms*, 9, 12
- Miller-Jones, J. C. A., Bahramian, A., Orosz, J. A., et al. 2021, *Science*, 371, 1046
- Miškovičová, I., Hell, N., Hanke, M., et al. 2016, *A&A*, 590, A114
- Mizumoto, M. & Ebisawa, K. 2017, *MNRAS*, 466, 3259
- Nandra, K., Barret, D., Barcons, X., et al. 2013, *arXiv e-prints*, arXiv:1306.2307
- Ness, J. U., Schaefer, B. E., Dobrotka, A., et al. 2012, *ApJ*, 745, 43
- Nowak, M. A., Hanke, M., Trowbridge, S. N., et al. 2011, *ApJ*, 728, 13
- Orosz, J. A., McClintock, J. E., Aufdenberg, J. P., et al. 2011, *ApJ*, 742, 84
- Oskinova, L. M., Feldmeier, A., & Kretschmar, P. 2012, *MNRAS*, 421, 2820
- Owocki, S. P., Castor, J. I., & Rybicki, G. B. 1988, *ApJ*, 335, 914
- Owocki, S. P. & Rybicki, G. B. 1984, *ApJ*, 284, 337
- Parker, M. L., Alston, W. N., Buisson, D. J. K., et al. 2017a, *MNRAS*, 469, 1553
- Parker, M. L., Alston, W. N., Igo, Z., & Fabian, A. C. 2020, *MNRAS*, 492, 1363
- Parker, M. L., Pinto, C., Fabian, A. C., et al. 2017b, *Nature*, 543, 83
- Parker, M. L., Reeves, J. N., Matzeu, G. A., Buisson, D. J. K., & Fabian, A. C. 2018, *MNRAS*, 474, 108
- Parker, M. L., Tomsick, J. A., Miller, J. M., et al. 2015, *ApJ*, 808, 9
- Perucho, M. & Bosch-Ramon, V. 2012, *A&A*, 539, A57
- Pinto, C., Alston, W., Parker, M. L., et al. 2018, *MNRAS*, 476, 1021
- Puls, J., Sundqvist, J. O., & Markova, N. 2015, in *New Windows on Massive Stars*, ed. G. Meynet, C. Georgy, J. Groh, & P. Stee, Vol. 307, 25–36
- Puls, J., Vink, J. S., & Najarro, F. 2008, *A&A Rev.*, 16, 209
- Sander, A. A. C., Fürst, F., Kretschmar, P., et al. 2018, *A&A*, 610, A60
- Sander, A. A. C., Hamann, W. R., Todt, H., Hainich, R., & Shenar, T. 2017, *A&A*, 603, A86
- Sundqvist, J. O., Björklund, R., Puls, J., & Najarro, F. 2019, *A&A*, 632, A126
- Sundqvist, J. O., Owocki, S. P., & Puls, J. 2012, in *Astronomical Society of the Pacific Conference Series*, Vol. 465, *Proceedings of a Scientific Meeting in Honor of Anthony F. J. Moffat*, ed. L. Drissen, C. Robert, N. St-Louis, & A. F. J. Moffat, 119
- Sundqvist, J. O., Owocki, S. P., & Puls, J. 2018, *A&A*, 611, A17
- Sundqvist, J. O. & Puls, J. 2018, *A&A*, 619, A59
- Tarter, C. B., Tucker, W. H., & Salpeter, E. E. 1969, *ApJ*, 156, 943
- Tashiro, M., Maejima, H., Toda, K., et al. 2018, in *Society of Photo-Optical Instrumentation Engineers (SPIE) Conference Series*, Vol. 10699, *Space Telescopes and Instrumentation 2018: Ultraviolet to Gamma Ray*, ed. J.-W. A. den Herder, S. Nikzad, & K. Nakazawa, 1069922
- Tombesi, F., Cappi, M., Yaqoob, T., et al. 2010, in *Astronomical Society of the Pacific Conference Series*, Vol. 427, *Accretion and Ejection in AGN: a Global View*, ed. L. Maraschi, G. Ghisellini, R. Della Ceca, & F. Tavecchio, 120
- Tomsick, J. A., Nowak, M. A., Parker, M., et al. 2014, *ApJ*, 780, 78
- Tomsick, J. A., Parker, M. L., García, J. A., et al. 2018, *ApJ*, 855, 3
- Vaughan, S., Edelson, R., Warwick, R. S., & Uttley, P. 2003, *MNRAS*, 345, 1271
- Verner, D. A., Verner, E. M., & Ferland, G. J. 1996, *Atomic Data and Nuclear Data Tables*, 64, 1
- Walborn, N. R. 1973, *ApJ*, 179, L123
- Walton, D. J., Tomsick, J. A., Madsen, K. K., et al. 2016, *ApJ*, 826, 87
- Webster, B. L. & Murdin, P. 1972, *Nature*, 235, 37
- Wilms, J., Nowak, M. A., Pottschmidt, K., Pooley, G. G., & Fritz, S. 2006, *A&A*, 447, 245

Appendix A: Filtering CCD gaps and dead pixel rows

In Sect. 3, we briefly discussed that the dither in *Chandra* introduces a systematic increase in F_{var}^2 around CCD gaps and rows of dead pixels. In this appendix, we explain in detail how affected wavelength bins are identified.

Figure A.1 (a) shows the distribution of counts on *Chandra*'s ACIS-S detector for Obs. 11044. The ACIS-S consists of a row of six quadratic CCDs, on which photons are dispersed by the HEG and MEG, resulting in a cross-like shape. Due to this design, a small amount of photons are lost at the boundaries between CCDs, in the so-called CCD gaps (Garmire et al. 2003). Rows of dead pixels have the same effect. We jointly refer to CCD gaps and dead rows as gaps in the following. To avoid the photon loss exclusively affecting specific wavelengths, the telescope pointing moves in a Lissajous pattern, periodically changing the zeroth order position on the detector, which averages the loss over a small wavelength range (Garmire et al. 2003). As a secondary effect, the number of detected photons strongly varies with time in range of a gap, which strongly affects variability analyses. The diagonal positioning of the gratings increases the affected range, because it causes one gap to affect a range of wavelengths at any given moment.

To account for the systematic variability introduced by the dither, we exclude all bins within dither range of gaps. The first steps towards identifying these bins is finding the positions of all gaps, by searching for pixel rows with zero counts along the x -coordinate of the detector, considering all events within 2–14.5Å. In this range, the number of counts per pixel is high enough to conclude that pixel rows with zero counts are likely an instrumental effect and not due to low signal. The detected gaps run across both the HEG and MEG spectrum, also indicating that they are instrumental.

A total of ~ 70 coinciding gaps were detected in Obs. 11044 and 3814, including the CCD gaps, whose positions were correctly reproduced. Eight additional gaps were picked up by the algorithm in Obs. 11044, but not in 3814, despite being visible by eye at coinciding positions. We therefore add these gaps in by hand in Obs. 3814. The detected gaps were verified by comparing them to the positions of dead rows documented in the ACIS badpix calibration file. As shown in Fig. A (c), all dead rows in the investigated range were found and have matching width. Note that the coloured region centred at ~ 3300 pixels is excluded from the analysis, because it contains zeroth order and $\lambda < 2\text{\AA}$ events, not because of a defective chip section.

The second step is to identify all wavelength bins which are in dither range of gaps. For each gratings arm, we calculate the minimal and maximal x position of all events in a given bin and check if the closest gap is at least a two pixel distance below the minimal or above the maximal value. If not, the bin is discarded. By requiring a distance of at least two pixels, we correctly reject bins that are half covered by a gap, which cannot be distinguished from bins directly adjacent to a gap.

As an example, a result of this selection is shown in Fig. A.1 (b) and (d) for the first order MEG spectrum. In panel (b), the spread of all bins that passed the filtering is shown in transparent blue and the gaps are marked in red. As intended, the filtered bins do not overlap with the gaps. Panel (d) compares the filtered and unfiltered F_{var}^2 spectra. CCD gaps cause huge, often double-peaked spikes. The shape results from the fact that the amount of arriving photons varies more strongly for bins around the gap edge than for bins largely covered the gap. Dead pixel rows give rise to smaller features because they are narrower. The

filtering algorithm succeeds in cutting out the large CCD gap spike, as well as several smaller ones caused by the gaps indicated in the figure above.

Figure A.1 (e) shows the effect of filtering on the number of counts available for the analysis in each wavelength bin. Depending on how the filtered wavelengths align across the gratings arms, the number of counts fluctuates greatly. In a small number of bins no signal is left, which results in the gaps in the data in Fig. 2. Note that the slightly visible two hump structure is a result of *Chandra*'s effective area (compare to, e.g., Canizares et al. 2005) and that the higher number of counts in Obs. 3814 is due to a higher exposure time.

Appendix B: Estimating binning variability

The *Chandra* ACIS-S detector has a read-out time of the order of seconds (Garmire et al. 2003), which not only limits its timing resolution, but also introduces systematic variability if the data are binned. Intuitively, some photons are assigned to time bin $n + 1$ instead of n , because of the delay between photon arrival and read-out.

We estimate the magnitude of this effect with Monte Carlo Simulations. We generate a random constant light curve by drawing photon arrival times from a constant distribution, separately for each observation, order, and grating, with their respective count numbers and exposure times. The read-out is simulated by rounding up the arrival times to the next larger time stamp present in the data, imprinting the read-out times from the observation on the simulated data. Note that the average count rates of Cyg X-1 in Obs. 11044 and 3814 are ~ 90 and ~ 70 cts s^{-1} , respectively, which makes it very unlikely that this approach misses read-out cycles because no photons arrived. We confirm this assumption by checking that there are no significant outliers in the time differences between consecutive events that exceed the read-out time. For each observation, order, and grating, we repeat this procedure 100 times and average the resulting total F_{var}^2 . Combining all gratings and orders as described in Sect. 3.3 yields the systematic binning variability, $F_{\text{var, binning}}^2$. The one sigma error on $F_{\text{var, binning}}^2$ is below $2 \cdot 10^{-4}$, for both Obs. 3814 and 11044.

An example of the simulation for Obs. 11044 is shown in Fig. B.1 as a function of binning time step. $F_{\text{var, binning}}^2$ strongly increases as the bin size approaches the read-out time, which is expected, as a smaller binning is more sensitive to a disturbance of a fixed magnitude. The periodicity in the ratio is caused by the binning time step matching an integer multiple of the duration of a read-out cycle. For a time step of 500 s, which was chosen for Fig. 2, $F_{\text{var, binning}}^2$ is below 0.9% of the total variability over the 2–14Å band in Obs. 11044. For Obs. 3814, we investigate time steps as short as 50 s, but due to the higher variability of this observation, the fraction stays below 0.3%. In absolute terms, $F_{\text{var, binning}}^2$ always stays below $2.5 \cdot 10^{-5}$ for time steps above 500 s in Obs. 11044 and below $2.7 \cdot 10^{-4}$ for time steps above 50 s in Obs. 3814 at a one sigma confidence.

We therefore conclude that $F_{\text{var, binning}}^2$ does not significantly impact our analysis, but note that the effect generally should be considered when investigating the excess variance at a timing resolution approaching the read-out time of the instrument.

Appendix C: Detailed F_{var}^2 spectrum of Obs. 11044

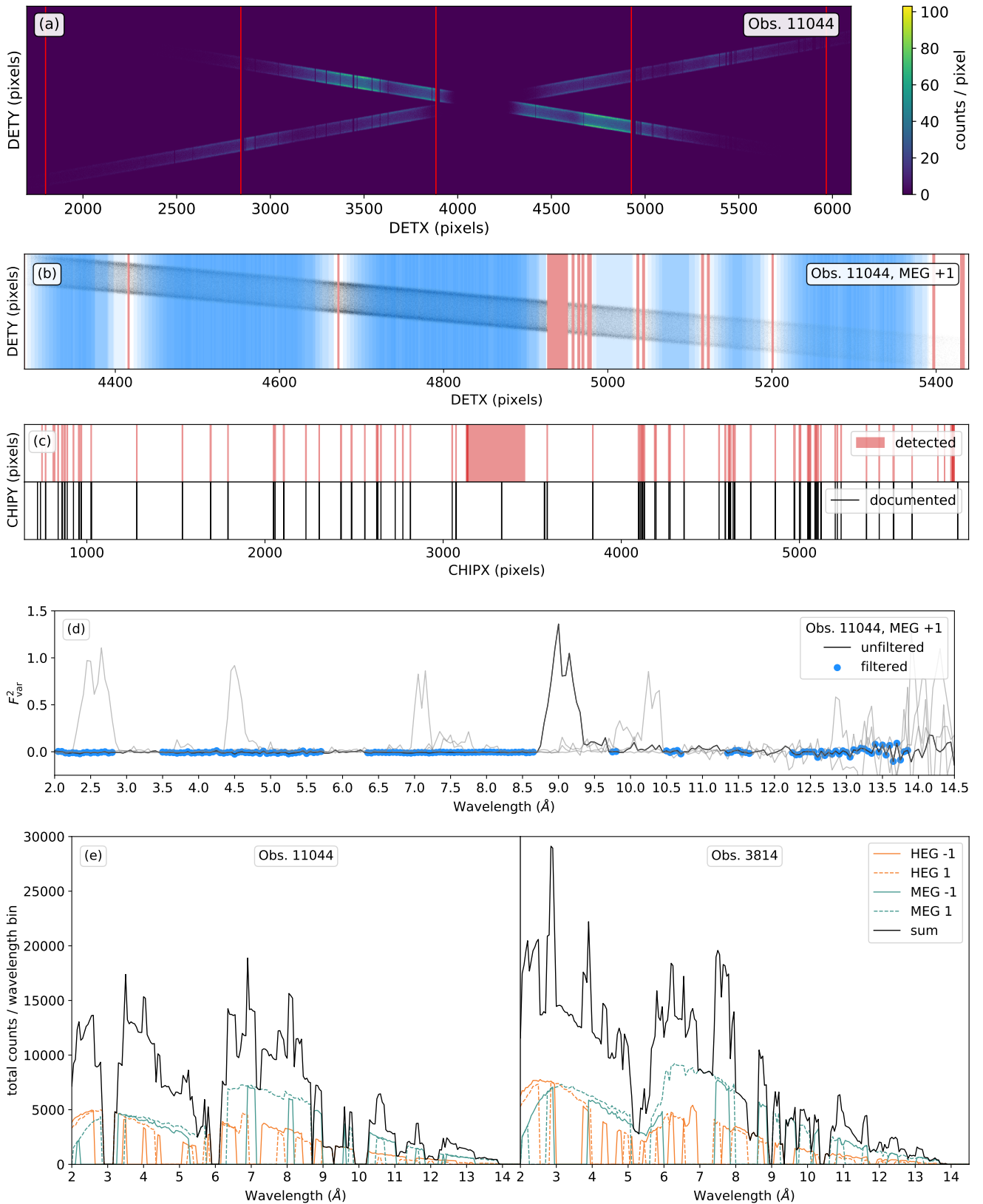


Fig. A.1: CCD gaps and dead pixel rows in *Chandra*'s ACIS-S detector are a major source of systematic variance. This figure illustrates our filtering procedure. (a) The distribution of counts on the ACIS-S CCD array, against which CCD gaps (marked in red) and dead pixel rows clearly stand out. Panel (b) shows the filtered bins (blue) and gaps (red) as an overlay on a cut-out of the top panel (first order MEG spectrum). Only bins with a minimum distance of two pixels to the detected gaps pass the filtering. Panel (c) compares the positions of detected gaps to those of dead pixel rows documented in the ACIS badpix calibration file. The gap at ~ 3300 pixels is not excluded because of a detector defect, but because it contains zeroth order and $\lambda < 2\text{\AA}$ events. In panel (d), the resulting F^2_{var} is shown, with the filtered bins highlighted in blue and MEG -1 and HEG ± 1 spectra (all light gray) for comparison. Details on the filtering procedure can be found in the text. (e) Total counts per wavelength bin in Obs. 11044 (left) and 3814 (right) after filtering, for all gratings arms (orange and green, straight and dashed lines) and their sum (black line). For clarity, data in panels (d) and (e) are displayed with lines and no errors are given.

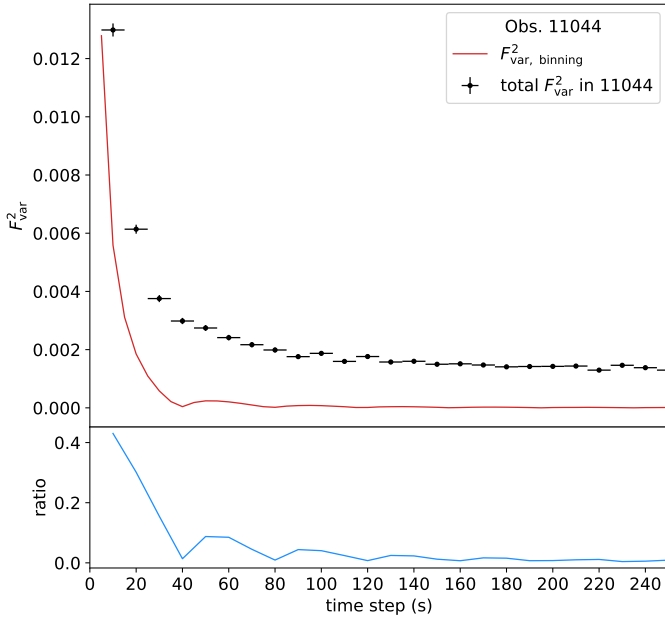


Fig. B.1: Systematic variability, F_{var}^2 , binning, introduced by the timing resolution of the ACIS detector (red line) compared to total F_{var}^2 in the broad band (2–14 Å, black data points) and their ratio, shown in the bottom panel. As a time step of 500 s is used for Obs. 11044, the effect is negligible in our analysis.

Table C.1: List of spike features in the F_{var}^2 spectrum of Obs. 3814 with a significance $>2\sigma$ and associated lines, i.e., lines which have a distance of $<0.05\text{Å}$ to the features. The listed lines are compiled from the selection described in Sect. 3.4. An alignment of lines detected in the previous analysis of the data set by Miškovičová et al. (2016) was searched for, but not found. References are given below.

Spike [Å]	σ	Ion	Line	Wl. [Å]	Ref.
5.82	2.2	P xiv	f [em.]	5.836	3
		P xiv	i [em.]	5.790	3
8.23	2.0	Fe xxii	$2p^2 \rightarrow 2p5d$	8.283	1
		Fe xxiv	$2p \rightarrow 4d$	8.232	1
8.58	2.2	Fe xxi	$2p^2 \rightarrow 2p5d$	8.608	1
		Fe xxiii	$2p \rightarrow 4d$	8.604	1
		Fe xxi	$2p^2 \rightarrow 2p5d$	8.555	1
		Fe xxi	$2p^2 \rightarrow 2p5d$	8.553	1
		Fe xxiii	$2p \rightarrow 4d$	8.540	1
		Fe xxiii	$2p \rightarrow 4d$	8.539	1
		Fe xxiii	$2p \rightarrow 4d$	8.539	1
11.50	2.1	Ne ix	$1s \rightarrow 3p$	11.546	7
		Fe xviii	$2p^5 \rightarrow 2p^4d1$	11.539	1
		Fe xviii	$2p^5 \rightarrow 2p^4d$	11.524	1
		Fe xviii	$2p^5 \rightarrow 2p^4d$	11.511	1
		Fe xviii	$2p^5 \rightarrow 2p^4d$	11.508	1
		Fe xxii	$2s^22p \rightarrow 2s2p3p$	11.480	1
		Fe xxii	$2s^22p \rightarrow 2s2p3p$	11.471	1
Fe xxii	$2s^22p \rightarrow 2s2p3p$	11.460	1		

References: (1) AtomDB (<http://www.atomdb.org/>), (3) Drake 1988, (7) Liao et al. 2013. **Notes:** Lines listed multiple times with different wavelengths differ in the fine structure. Emission lines are marked with [em.]. Iron lines are exclusively from AtomDB.

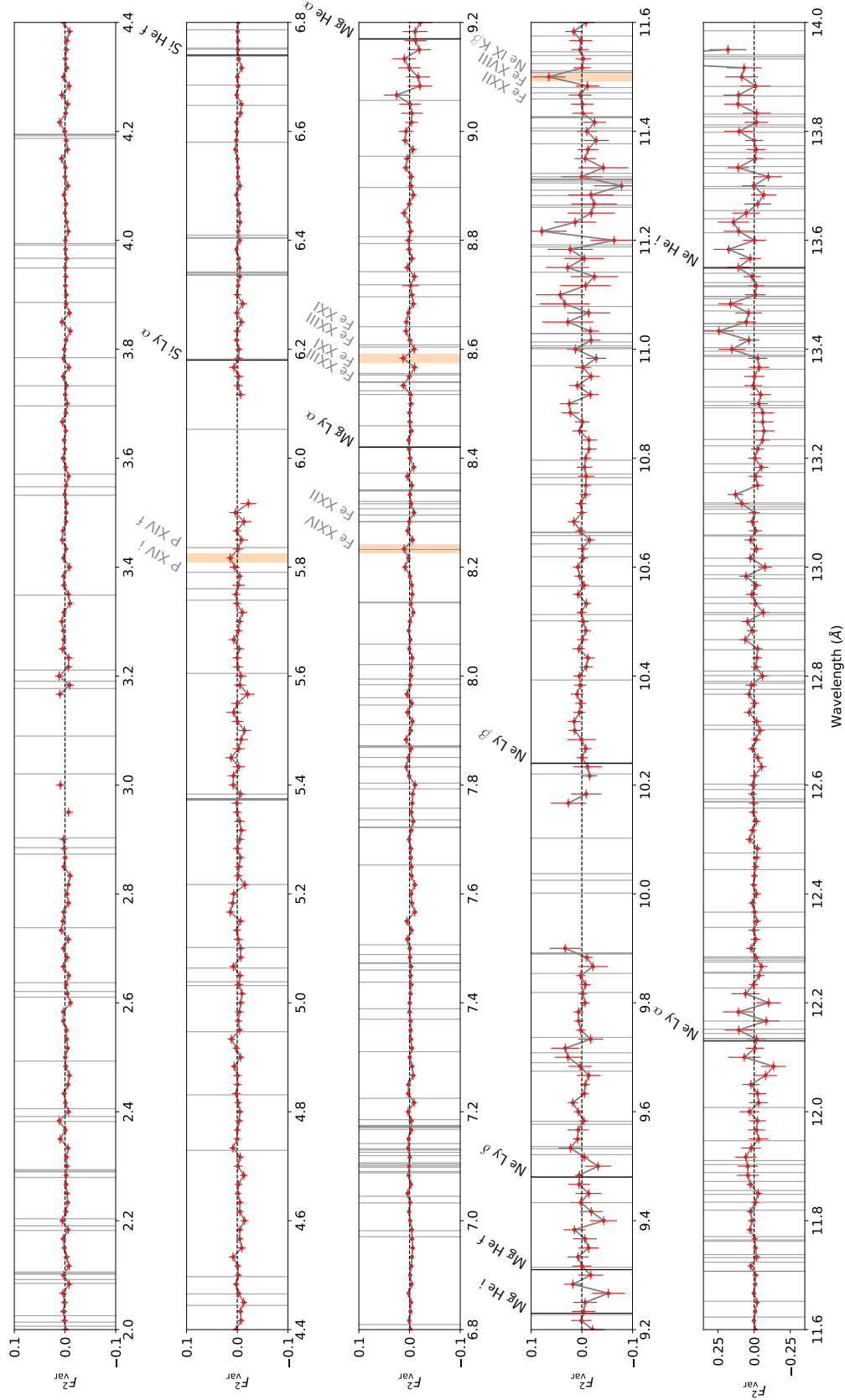


Fig. C.1: Detailed F^2_{var} spectrum of Obs. 11044, overlotted with the positions of line features identified in Miškovičová et al. (2016) (black) and transitions from the selection described in Sect. 3.4 (grey). Spikes with a significance $\sigma > 2\sigma$ are highlighted in orange. For subsequent iron transitions belonging to the same ion the label is shown only once. A list of spikes and associated transitions can be found in Tab. C.1. In contrast to Obs. 3814, the lines identified by Miškovičová et al. (2016) are P-Cygni profiles, which makes the absence of spike features plausible (see Sect. 5.4).